Modal Shape Analysis beyond Laplacian

Klaus Hildebrandt, Christian Schulz, Christoph von Tycowicz, Konrad Polthier

Abstract

In recent years, substantial progress in shape analysis has been achieved through methods that use the spectra and eigenfunctions of discrete Laplace operators. In this work, we study spectra and eigenfunctions of discrete differential operators that can serve as an alternative to the discrete Laplacians for applications in shape analysis. We construct such operators as the Hessians of surface energies or deformation energies. In particular, we design a quadratic energy such that, on the one hand, its Hessian equals the Laplace operator if the surface is a part of the Euclidean plane, and, on the other hand, the Hessian eigenfunctions are sensitive to the extrinsic curvature (*e.g.* sharp bends) on curved surfaces. Furthermore, we consider eigenvibrations induced by deformation energies, and we derive a closed form representation for the Hessian (at the rest state of the energy) for a general class of deformation energies. Based on these spectra and eigenmodes, we derive two shape signatures. One that measures the similarity of points on a surface, and another that can be used to identify features of surfaces.

1. Introduction

The spectrum and the eigenfunctions of the Laplace–Beltrami operator of a surface have stimulated much recent work in shape analysis and geometry processing, ranging from parametrization, segmentation, and symmetry detection to shape signatures and mesh filtering. Such methods profit from properties of the eigenfunctions of the Laplace–Beltrami operator. For example, on a curved surface they form an orthogonal basis of the space of L^2-functions on the surface. Furthermore, the Laplacian depends only on the metric of the surface, hence the eigenvalues and eigenfunctions are invariant under isometric deformations of the surface. However, there are disadvantages as well. For example, a consequence of the invariance to isometric deformations is an insensitivity to extrinsic features of the surface, like sharp bends, that are of essential importance for some applications.

Contributions. In this work we derive operators, whose eigenmodes and spectra can serve as alternatives to the spectrum and modes of the Laplacian for applications in geometry processing and shape analysis. On the one hand, the eigenfunctions of these operators share properties with the eigenfunctions of

the Laplacian, *e.g.*, they form an orthogonal basis of a space of variations of the surface. On the other hand, there are fundamental differences, *e.g.*, these eigenfunctions depend (not only on intrinsic quantities but also) on the extrinsic curvature of the surface. We consider two different settings: eigenvalues and eigenmodes of the Hessian of energies that are defined on a space of functions on a surface, and vibration modes and frequencies of surfaces derived from deformation energies.

The Dirichlet energy of a surface is a quadratic functional on an appropriate space of functions on a surface. The Hessian of this energy is the Laplace–Beltrami operator of the surface. We design a new energy by modifying the Dirichlet energy. The eigenfunctions of this energy are sensitive to the extrinsic curvature of the surface.

On a planar domain, the eigenfunctions of the Laplacian serve as a model for the vibration modes of a flat plate (Chladni plates). For curved surfaces more elaborate models are required to describe the vibration modes of a surface. We consider a physical model that describes vibration modes of a surface mesh through the eigenfunctions of the Hessian of a deformation energy. In general, computing the Hessian of a deformation energy is a delicate and laborious task. But, to compute the vibration modes we do not need to compute the Hessian at all points in the space of possible surfaces, but only at the point that represents the reference surface. We derive a simple formula that can be used to compute the Hessian at the reference surface for a general class of deformation energies. We hope that this framework will stimulate further exploration of the eigenmodes and eigenfrequencies of deformation energies.

As application, we propose two (multi-scale) signatures, the *vibration signature*, based on the vibration modes, and the *feature signature*, based on the eigenmodes of the modified Dirichlet energy. To each of the two signatures we associate a (multi-scale) pseudo-metric on the surface. The resulting *vibration distance* can be used as a similarity measure on the surface and the *feature distance* can identify features of a mesh. We prove a lemma that relates the vibration signature to the linearized gradient flow of the deformation energy. This gives further insight on the choice of the weights for the signature and reveals the geometry behind the signature.

Related work. Recently, we have seen a boom of papers that use the eigenvalues and eigenfunctions of the Laplace–Beltrami operator as an ingredient in algorithms in geometry processing and shape analysis. An overview of this development can be found in the recent survey by Zhang et al. (2010) and in the course notes of a *Siggraph Asia 2009* course held by Lévy and Zhang (2009). Here, we can only briefly outline the work that has been most relevant for this paper.

The spectrum of the Laplace–Beltrami operator of a Riemannian manifold contains a significant amount of information about the manifold and the metric. Though it does not fully determine the Riemannian manifold, it can be used as a powerful shape descriptor of a class of isometric Riemannian manifolds. Reuter et al. (2005, 2006) use the spectrum of the Laplace–Beltrami operator to con-

struct a fingerprint of surfaces, which they call the *Shape-DNA*. By construction this fingerprint is invariant under isometric deformations of a surface. Among other applications the Shape-DNA can be used for shape matching, copyright protection, and database retrieval. Rustamov (2007) developed the *Global Point Signature (GPS)*, a signature that can be used to classify shapes up to isometry. Based on the GPS, Ovsjanikov et al. (2008) developed a method for the detection of global symmetries in shapes. Dong et al. (2006) present an elegant technique that uses the Morse–Smale complex (and the quasi-dual complex) of a carefully chosen Laplace eigenfunction to generate a coarse quadrangulation of a surface mesh. This approach was extended by Huang et al. (2008), who design a least-squares optimization routine that modifies the selected Laplace eigenfunction (and hence its Morse–Smale complex) and provides a user with control of the shape, size, orientation, and feature alignment of the faces of the resulting quadrangulation. The computation of the spectrum and eigenfunctions of the Laplacian is a delicate and computationally expensive task, even for medium sized meshes. Vallet and Lévy (2008) propose an efficient shift-and-invert Lanczos method and present an implementation that is designed to handle even large meshes. Using the eigenfunctions of the Laplacian, one can compute the heat kernel of the surface. Sun et al. (2009) propose the heat kernel signature, a surface signature based on the heat kernel which they use to derive a measure for the geometric similarity of different regions of the surface. Due to its construction, this measure is invariant under isometric deformations of the surface. Independent of this work, Gebal et al. (2009) propose a similar signature, named the *Auto Diffusion Function*, and use it for mesh skeletonization and segmentation. In the context of shape matching and retrieval, Dey et al. (2010) use persistent extrema of the heat kernel signature to construct a robust and efficient pose-oblivious matching algorithm for 3D shapes. Given a corresponding pair of points on two shapes, Ovsjanikov et al. (2010) use the heat kernel to construct an isometric map between the shapes which allows them to find intrinsic symmetries and match partial, incomplete or isometrically deformed shapes.

Modal analysis is a well-established technique in structural mechanics and mechanical engineering that aims at computing the modes and frequencies of an object during vibration. In graphics, it is mainly used to speed up physical simulations, see Pentland and Williams (1989); Hauser et al. (2003); Barbič and James (2005); Choi and Ko (2005). Recently, Huang et al. (2009) use vibration modes of a surface to decompose it into physically meaningful parts. They compute the modes of the surface from the Hessian of a simplification of the *as-rigid-as-possible* deformation energy, which was proposed by Sorkine and Alexa (2007).

In physical simulation, thin shell models describe the dynamics of a thin flexible structure that has a curved undeformed configuration. For example, in cloth simulation thin shells are used to describe folds and wrinkles Bridson et al. (2003). Common discrete models Baraff and Witkin (1998); Bridson et al. (2003); Grinspun et al. (2003); Garg et al. (2007) describe the middle surface of a thin shell by a mesh and measure the bending of the surface at the edges

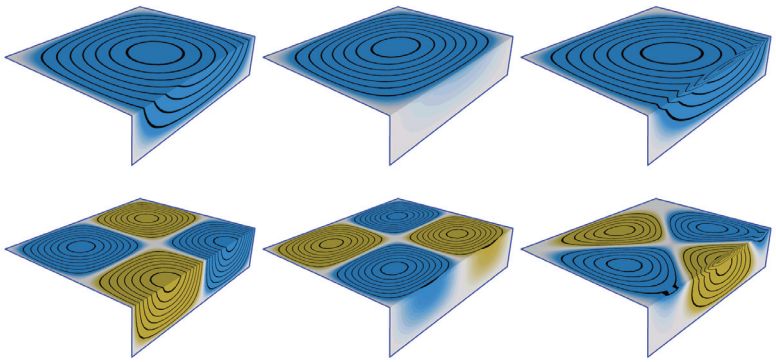

Figure 1: Visualization of modes of different energies. First column shows the Laplacian eigenmodes, second column the eigenmodes of the modified Dirichlet energy E_D^N, and third column the vibrations modes derived from the thin shell energy restricted to normal variations.

of the mesh. Of particular interest for this work is the model of Grinspun et al. (2003) that uses a discrete energy to simulate thin shells.

2. Laplace Modes and Spectrum

In this section, we briefly review the eigenvalue problem of the Laplacian on surfaces. We first state a weak form of the problem for smooth surfaces and then the discrete problem for surface meshes.

Let Σ be a smooth, compact surface in $\mathbb{R}^3$, and let H^1 denote the Sobolev space of weakly differentiable functions on Σ. On H^1 we consider the two bilinear forms

$$\langle f, g \rangle_{L^2} = \int_\Sigma f\, g \, \mathrm{d}A \qquad \text{and} \qquad \langle f, g \rangle_{H_0^1} = \int_\Sigma \langle \operatorname{grad} f, \operatorname{grad} g \rangle_\Sigma \, \mathrm{d}A. \tag{1}$$

Then, the eigenvalue problem for the Laplacian can be written in the following weak form: find all pairs $(\lambda, \phi) \in \mathbb{R} \times H^1$ such that

$$\langle \phi, \sigma \rangle_{H_0^1} = \lambda \, \langle \phi, \sigma \rangle_{L^2} \tag{2}$$

holds for all $\sigma \in H^1$.

In the discrete setting, we look at surface meshes in $\mathbb{R}^3$ and on a mesh x we consider the finite dimensional space F_x consisting of functions that are continuous and linear in every triangle. The bilinear forms $\langle \cdot, \cdot \rangle_{L^2}$ and $\langle \cdot, \cdot \rangle_{H_0^1}$ are well defined on F_x, see Dziuk (1988) and Hildebrandt et al. (2006), and can be evaluated by splitting the integrals into a sum over the triangles T of x:

$$\langle u, v \rangle_{L^2} = \sum_{T \in x} \int_T u\, v \, \mathrm{d}A \qquad \text{and} \qquad \langle u, v \rangle_{H_0^1} = \sum_{T \in x} \int_T \langle \operatorname{grad} u, \operatorname{grad} v \rangle_\Sigma \, \mathrm{d}A. \tag{3}$$

A function in F_x is determined by its function values at the vertices v_i of x, and the Lagrange basis (or nodal basis) of F_x is formed by the functions $\varphi_i \in F_x$ that take the value one at the vertex v_i and vanish at all other vertices. The matrix representations of $\langle \cdot, \cdot \rangle_{L^2}$ and $\langle \cdot, \cdot \rangle_{H^1_0}$ with respect to the Lagrange basis are the mass matrix M and the stiffness matrix S, which have the entries

$$M_{ij} = \langle \varphi_i, \varphi_j \rangle_{L^2} \qquad \text{and} \qquad S_{ij} = \langle \varphi_i, \varphi_j \rangle_{H^1_0} . \tag{4}$$

Explicit representations of the matrices M and S can be found in Pinkall and Polthier (1993), Wardetzky et al. (2007), and Vallet and Lévy (2008). The discretization of the eigenvalue problem (2) is: find all pairs $(\lambda, \phi) \in \mathbb{R} \times F_x$ such that

$$S\,\phi = \lambda M\,\phi \tag{5}$$

holds. This is a generalized eigenvalue problem for (possibly large) sparse matrices. Fast solvers for this problem are discussed in Saad (1992); Vallet and Lévy (2008) and an example of a software package that specializes in such problems is Arpack (see Lehoucq et al. (1998)). Since S is symmetric and M is positive definite, all eigenvalues of (5) are real and there exists and L^2-orthonormal basis of F_x consisting of eigenvectors.

It is common practice to replace the mass matrix M by a diagonal matrix with entries corresponding to the sum of the entries of each row of M. This is called mass lumping, see Wardetzky et al. (2007) for more details on the construction of mass matrices. In the following, we will always consider the diagonal lumped mass matrix, and we refer to the ith diagonal entry as the mass of the vertex v_i. The lumped mass matrix remains a symmetric and positive definite matrix. Hence the eigenvalue problem (5) with the lumped mass matrix has real eigenvalues, and we can always find an orthonormal basis of F_x consisting of eigenvectors of (5), where orthonormality is now measured with the scalar product on F_x given by the lumped mass matrix.

3. Modes of Surface Energies

In this section, we consider the modes and spectrum of the Hessian of surface energies. We show that the Laplacian eigenvalue problem appears as the eigenvalue problem of the Hessian of the Dirichlet energy. Based on this, we construct a new energy, a modified Dirichlet energy, that unlike the Dirichlet energy is sensitive to the extrinsic curvature of the surface, and we investigate the modes of this energy.

By a surface energy we mean a twice continuously differentiable function $E : F_x \to \mathbb{R}$. We are interested in the Hessian of E at minima m of E. At a minimum the gradient of the energy vanishes and the eigenmodes associated to the low eigenvalues of the Hessian of E point into the direction that locally cause the least increase of energy. The Hessian of E depends on the second derivatives of E and the scalar product on F_x, which in our case is the L^2-product. For

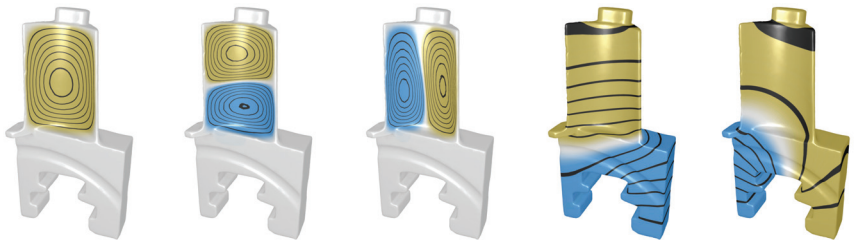

Figure 2: A qualitative comparison of modes of the modified Dirichlet energy and modes of the Laplacian is shown. The three models on the left show lower modes of the modified Dirichlet energy, which respect the extrinsic features, and the two rightmost models illustrate two lower modes of the Laplacian.

$u, v \in F_x$ let $D^2E_m(u, v)$ be the second derivative at m in direction u and v. Then, the Hessian at $m \in F_x$ is the operator $\mathrm{hess}_m E : F_x \to F_x$ given by

$$\langle \mathrm{hess}_m E\, u, v \rangle_{L^2} = D^2E_m(u, v) \tag{6}$$

for all $u, v \in F_x$. With respect to the Lagrange basis of F_x, $\mathrm{hess}_m E$ has the following matrix representation

$$\mathrm{hess}_m E = M^{-1}\partial^2 E_m,$$

where $\partial^2 E_m$ be the symmetric matrix containing the second partial derivatives at m and M is the mass matrix.

Eigenvalue problem. The eigenmodes and eigenvalues of the energy E at m are the solutions $(\lambda, \phi) \in \mathbb{R} \times F_x$ of the generalized eigenvalue problem

$$\partial^2 E_m\, \phi = \lambda M\, \phi. \tag{7}$$

Since $\mathrm{hess}_m E$ is self-adjoint with respect to the discrete L^2-product, all eigenvalues of $\mathrm{hess}_m E$, *i.e.* the solutions of (7), are real and there is an L^2-orthonormal basis of F_x that consists of eigenmodes $\mathrm{hess}_m E$. In such a basis, the matrix representation of D^2E_m and of $\langle \cdot, \cdot \rangle_{L^2}$ are diagonal matrices. Furthermore, the matrix $\partial^2 E_m$ is positive semi-definite (m is a minimum) which implies that the eigenvalues of (7) are non-negative.

Dirichlet energy. An example of such an energy is the discrete Dirichlet energy. For a compact smooth surface Σ, the Dirichlet energy is defined for weakly differentiable functions $\sigma : \Sigma \to \mathbb{R}$ (that vanish at the boundary of Σ) by

$$E_\Delta(\sigma) = \frac{1}{2} \langle \sigma, \sigma \rangle_{H^1_0}. \tag{8}$$

Then, the discrete Dirichlet energy on a mesh x is defined for functions $u \in F_x$ by

$$E_D(u) = \frac{1}{2} u^T S\, u, \tag{9}$$

where S is the stiffness matrix of eq. (4). For a rigorous treatment of this discrete Dirichlet energy and a convergence analysis see Dziuk (1988); Hildebrandt et al. (2006). The minima of E_D are the constant functions in F_x. The Dirichlet energy is a quadratic functional and therefore has a constant Hessian. At any point, $\partial^2 E$ equals S and (7) is the Laplace eigenvalue problem.

Modified Dirichlet energy. Assume that Σ is an orientable smooth surface in $\mathbb{R}^3$ and let ν denote the normal of Σ. Then, all three coordinates ν^k of ν are smooth functions and for a weakly differentiable function φ the product $\varphi\,\nu^k$ is weakly differentiable. We define

$$E_\Delta^N(\varphi) = \sum_{k=1}^{3} E_\Delta(\varphi\,\nu^k). \tag{10}$$

This energy satisfies the equation

$$E_\Delta^N(\varphi) = E_\Delta(\varphi) + \frac{1}{2}\int_\Sigma \varphi^2(\kappa_1^2+\kappa_2^2)\mathrm{d}A, \tag{11}$$

where κ_1 and κ_2 are the principal curvatures of Σ. This means that $E_D^N(\varphi)$ is the sum of the Dirichlet energy of φ and the φ^2-weighted total curvature of Σ.

To discretize the energy E_Δ^N we fix a normal direction at every vertex of the mesh, and we denote the oriented unit normal vector at a vertex v_i by $N(v_i)$. Then, we say a continuous and piecewise linear vector field V on x is a *normal vector field* if for every vertex v_i of x the vector $V(v_i)$ is parallel to $N(v_i)$. The space of normal vector fields on x is an n-dimensional vector space and the map that maps a function $u \in F_x$ to the normal variation V_u, given by $V_u(v_i) = u(v_i)\,N(v_i)$ for all $v_i \in x$, is a linear isomorphism. The three coordinate functions V_u^k of V_u are functions in F_x and we define the discrete energy E_D^N analog to eq. (10) by

$$E_D^N(u) = \sum_{k=1}^{3} E_D(V_u^k).$$

A simple calculation shows that the energy E_D^N satisfies

$$E_D^N(u) = \frac{1}{2}u^T A\,u, \tag{12}$$

where the formula

$$A_{ij} = \langle N(v_i), N(v_j)\rangle\, S_{ij}$$

relates the entries A_{ij} of the matrix A to the entries S_{ij} of the cotan-matrix S.

Modes of E_D^N. As illustrated in Figures 1 and 3, the eigenmodes of E_D and E_D^N differ significantly. Whereas the eigenmodes of the Laplacian are insensitive to the extrinsic curvature, the modes of E_D^N corresponding to lower eigenvalues

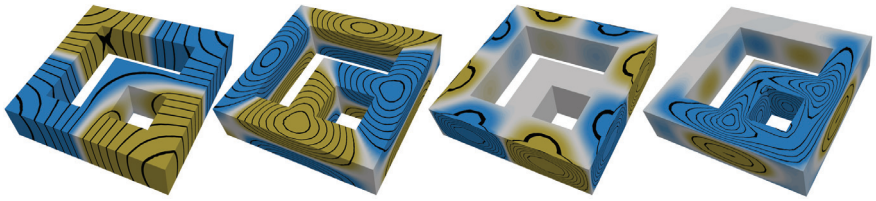

Figure 3: Two eigenmodes of the lower spectrum on the double torus with sharp features, left: Laplacian, and right: modified Dirichlet energy.

hardly move in regions of high curvature, see Fig 1. A possible explanation for this behavior is the following. The energy has its minimum at the origin of the space of normal vector fields. Therefore, at the origin the gradient of the energy vanishes and the modes of the Hessian corresponding to small eigenvalues point into directions of least expenditure of energy. Now, equation (11) shows that E_D and E_D^N differ by a term that measures a weighted L^2-norm of the function, where the weight is the sum of the squared principal curvatures. Therefore, eigenmodes of E_D^N that correspond to small eigenvalues have small function values in areas of high curvature, because then a variation in this direction causes less increase of energy.

4. Deformation Energies

In this section, we consider discrete deformation energies that are defined for surface meshes in $\mathbb{R}^3$. Such energies measure the deformation of a mesh from a reference mesh. A surface mesh is given by the positions of the vertices and the combinatorial information which vertices form triangles. Here, we vary only the positions of the vertices and leave the combinatorial information unchanged. The positions of the vertices can be written in one $3n$-vector x, where n is the number of vertices. Hence, we can identify the space of meshes (with fixed combinatorics) with $\mathbb{R}^{3n}$. We denote this space by X.

A general deformation energy. We consider deformation energies $E : X \mapsto \mathbb{R}$ of the following form:

$$E(x) = \frac{1}{2} \sum\nolimits_i \omega_i(\bar{x}) \left(f_i(x) - f_i(\bar{x})\right)^2 , \tag{13}$$

where x is a surface mesh and $\bar{x}$ a fixed reference mesh. In this equation, the sum can run over the edges, the vertices, or the triangles of x, and the f_i's and ω_i's are elementary functions, which *e.g.* measure angles, length of edges, or area of triangles. The weights ω_i must be positive and we require E to be twice continuously differentiable around $\bar{x}$. Then, E has a global minimum at $\bar{x}$, which implies that the gradient of E at $\bar{x}$ vanishes and that the Hessian of E at $\bar{x}$ is positive semi-definite.

As an example of such an energy we consider a discrete energy that is designed for thin shell simulation.

Discrete shells. If we regard the surface mesh as a thin shell, then a physical model of thin shells provides us with a deformation energy. Here, we consider the discrete shell model of Grinspun et al. (2003). The energy that governs this model of thin shells is a weighted sum of two components: a flexural energy and a membrane energy. The weights reflects properties of the material to be simulated, *e.g.*, in cloth simulation the membrane energy usually gets a high weight due to the stretching resistance of cloth.

The discrete flexural energy is given as a summation over the edges of the mesh:

$$E_F = \frac{3}{2} \sum\nolimits_i \frac{\|\bar{e}_i\|^2}{\bar{A}_{e_i}} \left(\theta_{e_i} - \bar{\theta}_{e_i}\right)^2, \tag{14}$$

where θ_{e_i} is the dihedral angle at the edge e_i, A_{e_i} is the combined area of the two triangles incident to e_i and $\|e_i\|$ is the length of the edge. The quantities $\|\bar{e}_i\|$, $\bar{A}_{e_i}$, and $\bar{\theta}_{e_i}$ are measured on the reference mesh. To write this flexural energy in the general form (13) we set

$$f_i(x) = \theta_{e_i} \quad \text{and} \quad \omega_i(x) = \frac{3\,\|e_i\|^2}{A_{e_i}}.$$

The membrane energy consists of two terms: one measuring the stretching of the edges,

$$E_L = \frac{1}{2} \sum\nolimits_i \frac{1}{\|\bar{e}_i\|} (\|e_i\| - \|\bar{e}_i\|)^2, \tag{15}$$

and one measuring the change of the triangle areas A_i

$$E_A = \frac{1}{2} \sum\nolimits_i \frac{1}{\bar{A}_i} (A_i - \bar{A}_i)^2. \tag{16}$$

Here the second sum runs over the triangles of the mesh. We can describe E_L in the general form (13) by setting

$$f_i(x) = \|e_i\| \quad \text{and} \quad \omega_i(x) = \frac{1}{\|e_i\|},$$

and to describe E_A we set

$$f_i(x) = A_i \quad \text{and} \quad \omega_i(x) = \frac{1}{A_i}.$$

5. Modes of Deformation Energies

Modal analysis provides ways to compute the modes of a surface with respect to a deformation energy. To inspect the modes of a mesh, given by a $3n$-vector $\bar{x}$, we consider a deformation energy $E(x)$ that has $\bar{x}$ as a reference surface. Then, we are interested in the eigenvalues and eigenmodes of the Hessian of the deformation energy E at the mesh $\bar{x} \in X$.

The Hessian of a deformation energy (or more generally of a function) does not depend solely on the differentiable structure of X, but also on the metric

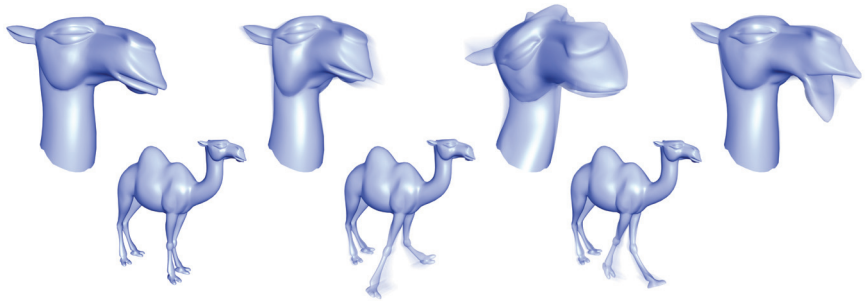

Figure 4: Visualization of vibration modes derived from the discrete thin shell energy. In each row the left most image shows the rest state followed by some deformations captured by a vibration mode.

on X, hence belongs to Riemannian geometry. Therefore, before considering the Hessian of E we equip X with a metric. Since X equals $\mathbb{R}^{3n}$, the tangent space T_xX at a mesh x can be identified with $\mathbb{R}^{3n}$. We can interpret an element of T_xX as a vector field on x, which assigns a vector in $\mathbb{R}^3$ to every vertex of x and is piecewise linearly interpolated in the triangles. Then, a natural choice of a scalar product on T_xX is the L^2-product of the piecewise linear vector fields. In the nodal basis, this product is represented by the mass matrix, see Section 2. Since the mass matrix depends on the mesh x, we denote the mass matrix, which represents the scalar product on T_xX with respect to the nodal basis by M_x. For completeness, we would like to mention that if x is a mesh that has degenerate triangles, the discrete L^2-product on T_xX may be only positive semi-definite. However, away from the closed set of meshes that have at least one degenerate triangle, X equipped with the discrete L^2-product is a Riemannian manifold. Using the L^2-product to obtain a metric on the shape space of a surface is a common choice, for example it is used for the numerical integration of gradient flows of geometric functionals like the area (mean curvature flow) or the Willmore energy, see Dziuk (1991); Clarenz et al. (2004). However, other choices of scalar products are possible as well. In Eckstein et al. (2007) gradient flows of geometric functionals with respect alternative choices of scalar products are explored.

We denote by ∂E_x the $3n$-vector containing the first partial derivatives of E at x and by $\partial^2 E_x$ the matrix containing the second partial derivatives at x. We would like to emphasize that ∂E_x and $\partial^2 E_x$ do not depend on the metric on X, whereas the gradient and the Hessian of E do. The gradient of E at x is given by

$$\operatorname{grad}_x E = M_x^{-1} \partial E_x. \tag{17}$$

The Hessian of E at a mesh x is the self-adjoint operator that maps any tangent vector $v \in T_xX$ to the tangent vector $\operatorname{hess}_x E(v) \in T_xX$ given by

$$\operatorname{hess}_x E(v) = \nabla_v \operatorname{grad}_x E, \tag{18}$$

where ∇ is the covariant derivative of X. We would like to remark that eq. (18)

reduces to eq. (6) in the case that the metric is constant.

Hessian computation. In general, it is a delicate task to derive an explicit representation of the Hessian of a deformation energy and often only approximations of the Hessian are available. Here, we derive a simple explicit formula for the Hessian of a deformation in the general form (13) at the point $\bar{x}$, which involves only first derivatives of the f_i's.

Since the gradient of E vanishes at $\bar{x}$, one can show that at $\bar{x}$ the Hessian of E takes the following form

$$\operatorname{hess}_{\bar{x}} E = M_{\bar{x}}^{-1} \partial^2 E_{\bar{x}}.$$

This immediatly follows from the representation of the Hessian in local coordinates, cf. (Jost, 2008, eq. 3.3.47, p. 152). Hence, at $\bar{x}$ we do not need derivatives of the metric to compute $\operatorname{hess}_{\bar{x}} E$. Furthermore, to compute the second partial derivatives of E at $\bar{x}$ we do not need to calculate second derivatives, but we only need the first derivatives of the f_i's. We present an explicit formula for $\partial^2 E_{\bar{x}}$ in the following Lemma, which follows from simple application of the product rule.

Lemma 1 (Explicit Hessian). *Let E be a deformation energy of the form (13). Then, the matrix $\partial^2 E_{\bar{x}}$ containing the second derivatives of E at $\bar{x}$ has the form*

$$\partial^2 E_{\bar{x}} = \sum\nolimits_i \omega_i(\bar{x})\, \partial f_{i\,\bar{x}}\, \partial f_{i\,\bar{x}}{}^T, \tag{19}$$

where $\partial f_{i\,\bar{x}}{}^T$ denotes the transpose of the vector $\partial f_{i\,\bar{x}}$.

The computation of the first derivatives of the f_i's is usually straightforward, and, in addition, the first derivatives of many elementary quantities are explicitly stated in the literature. For example, a formula for the first derivative of the dihedral angle θ can be found in Wardetzky et al. (2007) and a formula for the first derivative of the area of a triangle is contained in Polthier (2005).

Eigenvalue problem. To obtain the eigenmodes of $\operatorname{hess}_{\bar{x}} E$, we need to solve the generalized eigenvalue problem

$$\partial^2 E_{\bar{x}}\, \Phi = \lambda\, M_{\bar{x}}\, \Phi, \tag{20}$$

where $\Phi \in T_{\bar{x}} X$ and $\lambda \in \mathbb{R}$. The structure of (20) equals the structure of (7), thus the eigenvalues of (20) are real and the eigenmodes $\operatorname{hess}_{\bar{x}} E$ form an orthogonal basis of $T_{\bar{x}} X$.

Vibration modes and gradient flow. To illustrate the concept of eigenmodes of the Hessian of a deformation energy, we look at the vibrations of a mesh in a force field induced by the energy. For simplicity, we consider the case of free vibrations. In general, the dynamics of a time-dependent mesh $x(t)$ in the space X is governed by a system of non-linear second-order ODEs of the form

$$M_{x(t)} \ddot{x}(t) = f(t, x(t), \dot{x}(t)),$$

see Baraff and Witkin (1998). Here, the mass matrix M_x represents the physical mass of x and f represents the acting forces. We consider the force field that has E as its potential, *i.e.*,

$$f(t, x(t), \dot{x}(t)) = -\partial E_{x(t)}.$$

In the case of free vibrations, this is the only force. In a more general setting, we could include damping and exterior forces, see Pentland and Williams (1989). The equations that govern the motion of a time-dependent mesh $x(t)$ during free vibration are

$$\operatorname{grad}_{x(t)} E + \ddot{x}(t) = 0, \tag{21}$$

where we use the definition of the gradient, eq. (17), to simplify the formula. Since we are interested in meshes x that are (arbitrarily) close to $\bar{x}$, we expand the force $\operatorname{grad}_x E$ into a Taylor series around $\bar{x}$. Using $\partial E_{\bar{x}} = 0$ ($\bar{x}$ is a minimum of E) we get

$$\operatorname{grad}_x E = \operatorname{hess}_{\bar{x}} E(x - \bar{x}) + \mathcal{O}(\|x - \bar{x}\|^2). \tag{22}$$

Then, if we omit the second order term in (22) and plug (21) and (22) together, we get

$$\operatorname{hess}_{\bar{x}} E\, u(t) + \ddot{u}(t) = 0, \tag{23}$$

where $u(t) = x(t) - \bar{x}$. This is a system of second-order linear ODEs that are coupled by $\operatorname{hess}_{\bar{x}} E$. To solve the system we consider a normalized eigenbasis B of $\operatorname{hess}_{\bar{x}} E$. Written in such a basis, both matrices $\partial^2 E_{\bar{x}}$ and $M_{\bar{x}}$ are diagonal matrices and equation (23) takes the form

$$\Lambda\, w(t) + \ddot{w}(t) = 0, \tag{24}$$

where w is the representation of u in the basis B and Λ is a diagonal matrix that contains the eigenvalues. The system (24) is decoupled and can be solved row by row. Each row describes an oscillation around $\bar{x}$ with frequency $\sqrt{\lambda}$ in the direction of the eigenmode Φ corresponding to the eigenvalue λ. This means, that the eigenmodes of problem (20) describe the vibration modes of the mesh $\bar{x}$ (with respect to the deformation energy E). The vibrations of a physical system are usually not free, but are affected by damping forces. Common models for such forces are Rayleigh damping, see Hauser et al. (2003), and, even simpler, mass damping, see Pentland and Williams (1989). We would like to mention that if Rayleigh (or mass) damping forces are added to the system, it still has the same vibration modes, see Hauser et al. (2003).

The gradient flow of the energy E is given by the system

$$\operatorname{grad}_{x(t)} E + \dot{x}(t) = 0 \tag{25}$$

of first order ODEs. It describes the evolution of a surface in a velocity field given by the negative gradient of the energy. Initial data for the equation is a position of the mesh $x(t)$ for some time t_0. Using eq. (22), we derive the linearized gradient flow

$$\operatorname{hess}_{\bar{x}} E\, u(t) + \dot{u}(t) = 0. \tag{26}$$

Figure 5: Vibration distance to the marked vertex v of the Armadillo model in three colorings: continuous coloring from white being similar to red being dissimilar to v and binary colorings with two different thresholds where blue vertices are similar to v.

Analogously to eq. (23), this system can be decoupled using the eigenmodes of $\mathrm{hess}_{\bar{x}} E$.

6. Modal Signatures

In this section we introduce two multi-scale surface signatures: the *vibration signature*, based on the vibration modes of the surface with respect to the discrete shells energy, and the *feature signature*, which uses the eigenfunctions and eigenvalues of the modified discrete Dirichlet energy E_D^N. The construction of the signatures follows the construction of the heat kernel signature defined in Sun et al. (2009).

The signatures we consider are multi-scale signatures, which take a positive scale parameter t as input. For every t such a signature is a function on the mesh, *i.e.*, it associates a real value to every vertex of the mesh. Let v be a vertex of a mesh x and let t be a positive value. Then, we define the *vibration signature* of x at vertex v and scale t by

$$S_t^{Vib}(v) = \sum_j e^{-\lambda_j t} \left\| \Phi_j(v) \right\|_{\mathbb{R}^3}^2 , \tag{27}$$

where λ_j and Φ_j denote the eigenvalues and the L^2-normalized vector-valued vibration modes of a mesh x with respect to the discrete shells energy. The value $\left\| \Phi_j(v) \right\|_{\mathbb{R}^3}$ describes the displacement of the vertex v under the L^2-normalized vibration mode Φ_j. For a fixed t the vibration signature of v measures a weighted average displacement of the vertex over all vibration modes, where the weight of the j^{th} eigenmode is $e^{-\lambda_j t}$. The weights depend on the eigenvalues and on the scale parameter. For increasing λ, the function $e^{-\lambda t}$ rapidly decreases, *e.g.*, the modes with smaller eigenvalue receive higher weights than the modes with large eigenvalues. Furthermore, for increasing t all weights decrease, and, more importantly, the weights of the vibration modes with smaller eigenvalues increases relative to the weights of the modes with larger eigenvalues.

In addition to (27), the vibration signature can be computed using the linearized gradient flow, which we defined in eq. (26). Before we explain this point of view in the next lemma, we introduce some notation. Let $\{b_1, b_2, b_3\}$ be the standard basis of $\mathbb{R}^3$ and $\alpha \in \{1, 2, 3\}$. We denote by δ_α^v the vector field in T_xX that satisfies

$$\langle \delta_\alpha^v, \Phi \rangle_{L^2} = \langle \Phi(v), b_\alpha \rangle_{\mathbb{R}^3} . \tag{28}$$

for all $\Phi \in T_xX$. Explicitly δ_α^v is given by

$$\delta_\alpha^v = M_x^{-1} e_\alpha^v,$$

where e_α^v is the vector field on x that satisfies $e_\alpha^v(v) = b_\alpha$ and vanishes at all other vertices. If a diagonal mass matrix is used, then $\delta_\alpha^v = \frac{1}{m_v} e_\alpha^v$. Here m_v is the diagonal entry of the mass matrix corresponding to the vertex v; in the case of the lumped mass matrix, m_v is a third of the combined area of all triangles adjacent to v.

Lemma 2. *Let v be a vertex of x, and let $u_1(t), u_2(t)$, and $u_3(t)$ be the solutions of the linearized gradient flow equation (26) with initial values $u_\alpha(0) = \delta_\alpha^v$. Then, the vibration signature satisfies*

$$S_{2t}^{Vib}(v) = \sum_{\alpha=1}^{3} \|u_\alpha(t)\|_{L^2}^2 \tag{29}$$

for all t.

Proof. Using the vibration modes Φ_j we can derive the following explicit representation of the functions $u_\alpha(t)$:

$$u_\alpha(t) = \sum_j \langle \delta_\alpha^v, \Phi_j \rangle_{L^2} \, e^{-\lambda_j t} \Phi_j = \sum_j \langle \Phi_j(v), b_\alpha \rangle_{\mathbb{R}^3} \, e^{-\lambda_j t} \Phi_j,$$

where we use eq. (28) in the last equality. Then, from the property that the vibration modes Φ_j are orthonormal, we get

$$\sum_{\alpha=1}^{3} \|u_\alpha(t)\|_{L^2}^2 = \sum_j e^{-2\lambda_j t} \sum_{\alpha=1}^{3} \langle \Phi_j(v), b_\alpha \rangle_{\mathbb{R}^3}^2 = \sum_j e^{-2\lambda_j t} \, \|\Phi_j(v)\|^2 = S_{2t}^{Vib}(v),$$

which proves the lemma. ■

We can interpret the initial value condition $u_\alpha(0) = \delta_\alpha^v$ as an initial deformation of the surface. Then $u_\alpha(t)$ describes how this deformation evolves under the linearized gradient flow; for $t \to \infty$, the surface reaches the rest state of the energy. The signature measures for every t are the sum of the L^2-norms of $u_1(\frac{t}{2}), u_2(\frac{t}{2})$, and $u_3(\frac{t}{2})$. The signature is independent of the choice of an orthonormal basis $\{b_1, b_2, b_3\}$ in $\mathbb{R}^3$ (which determines the initial value conditions). The lemma gives a motivation for the choice of the weights $e^{-\lambda_j t}$, that appear in the definition of the vibration signature. Furthermore, the lemma

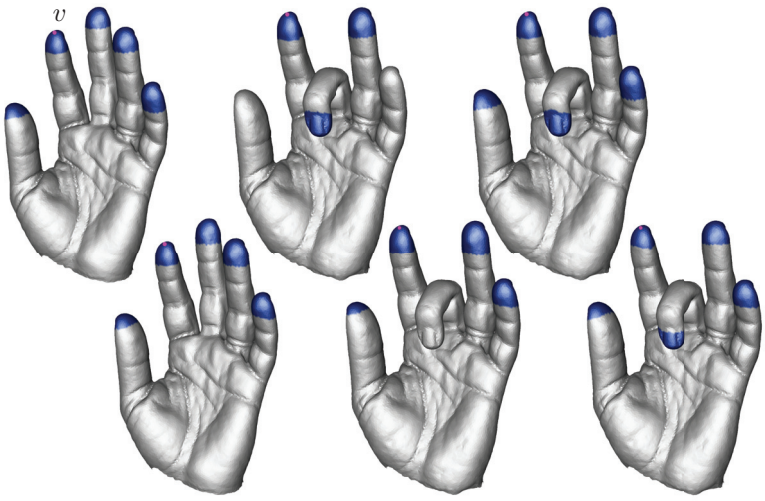

Figure 6: Vertices (blue) similar to vertex v based on heat kernel signature Sun et al. (2009) (top row) and our vibration signature (lower row). Left and right column depict similarity based on a small range of t's and middle column on a large range of t's.

shows that one can compute the signature without computing the eigenmodes and spectrum first. An algorithm based on eq. (29) would not be efficient for our purposes, since we would need to solve the diffusion equation for every vertex of the mesh. Still, if the goal is to evaluate the signature only at certain vertices or for small time values, a computation based eq. (29) can be more effective than a scheme that involves solving the eigenvalue problem.

The *feature signature* is constructed in a similar manner, but it uses the eigenmodes and eigenvalues of the modified Dirichlet energy E_D^N. We define

$$S_t^{Feat}(v) = \sum_j e^{-\lambda_j t}\, \phi_j(v)^2 \tag{30}$$

where the λ_j are the eigenvalues and the $\phi_j(v)$ are the L^2-normalized eigenmodes of the Hessian of the modified discrete Dirichlet energy E_D^N.

Multi-scale distances. From each of the two signatures we can construct the following (multi-scale) pseudo-metric on the mesh: let v,$\tilde{v}$ be vertices of the mesh x, then we define

$$\delta_{[t_1,t_2]}(v,\tilde{v}) = \left(\int_{t_1}^{t_2} \left(\frac{S_t(v) - S_t(\tilde{v})}{\sum_k e^{-\lambda_k t}} \right)^2 \mathrm{d}\log t \right)^{\frac{1}{2}}. \tag{31}$$

By construction, for any pair of scale values $t_1 < t_2$, $\delta_{[t_1,t_2]}$ is positive semi-definite and symmetric, and one can show that it satisfies the triangle inequality. We call the pseudo-metrics constructed from S_t^{Vib} and S_t^{Feat} the *vibration distance* and the *feature distance*.

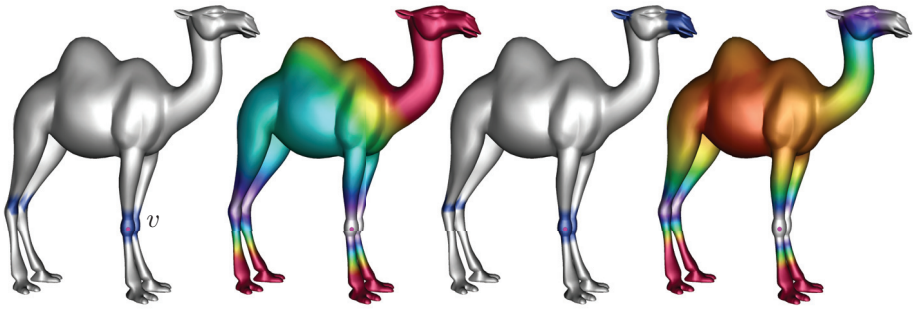

Figure 7: Comparison of two similarity measures. Distance to vertex v in binary as well as continuous coloring based on our vibration signature (left most) and the heat kernel signature (right most).

The idea behind the construction of the pseudo-metric is to use the integral $\int_{t_1}^{t_2} \left(S_t(v) - S_t(\tilde{v})\right)^2 \mathrm{d}t$. However, the actual definition additionally includes two heuristics. First, since for increasing t the values $S_t(v)$ decreases for all v, we normalize the value $S_t(v) - S_t(\tilde{v})$ by dividing it by the discrete L^1-norm of S_t,

$$\|S_t\|_{L^1} = \sum_k e^{-\lambda_k t}.$$

Second, for a fixed vertex v, the signature $S_t(v)$ varies more for small values of t compared to large t. To increase the discriminative power of the pseudo-metric, we associate a higher weight to the small t and a lower weight to the larger t. We achieved this by using a weighted integral with weight function $\mathrm{d}\log t = \frac{1}{t}\mathrm{d}t$. To discretize this weighted integral we use a uniform decomposition of the logarithmically scaled interval $[t_1, t_2]$.

7. Results and Discussion

We experiment with the vibration modes of the discrete thin shell energy, the eigenmodes of E_D^N, and, for comparison, the eigenfunctions of the *cotan*-Laplace operator. As a discrete L^2-scalar product we use the diagonal (or lumped) mass matrix M. The diagonal entry in the i^{th} row of the matrix is a third of the combined area of the triangles adjacent to the i^{th} vertex of the mesh. To compute the eigenmodes of a mesh, we solve the generalized eigenvalue problem (20). Since M is a diagonal matrix, this problem can be transformed into a standard eigenvalue problem as described in Vallet and Lévy (2008). Then, we solve the resulting standard eigenvalue problem with the shift-and-invert Lanczos scheme described in Vallet and Lévy (2008). For most examples and applications we do not need to compute the full spectrum, but only the lower part of the spectrum.

Spectral zoo. We compare the eigenmodes of the Laplacian to the ones of the modified Dirichlet energy E_D^N. In addition, we consider the modes we obtain

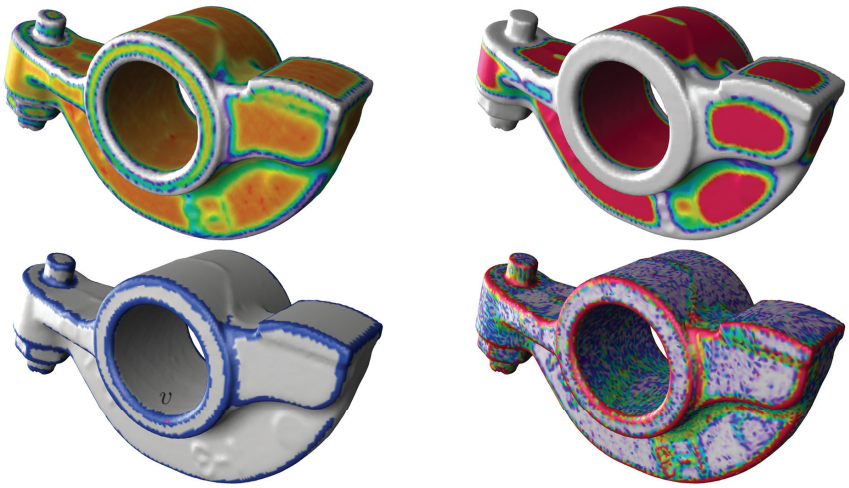

Figure 8: Results of the feature signature on the rocker arm model. The top row shows the feature signature for increasing scale values. The bottom row shows on the left the feature distance to the marked vertex v binary colored by a threshold, and, on the right, the surface colored by curvature ($\sqrt{\kappa_1^2 + \kappa_2^2}$).

when considering the discrete shells energy and allowing only normal variations of the mesh. Normal variations can be described by a functions on the mesh, which described the offset of every point. Therefore, we can visually compare the restricted eigenmodes to the eigenmodes of the Laplacian and the modified Dirichlet energy. To convey an impression of the characteristics of the modes of the different energies, we show some examples in Figures 1 and 3. To visualize the modes we use blue color for positive values, white for zero crossings, and orange for negative values. Additionally, we draw isolines as black lines.

As a first example, we study how the eigenmodes change when we isometrically deform a flat plate, see Fig. 1. On the undeformed flat plate, the eigenmodes of E_D^N equal the eigenmodes of the Laplacian. As shown in Fig. 1, there are certain differences between the three types of considered modes when computed on the deformed plate. Due to its intrinsic nature the Laplacian eigenmodes ignore the newly introduced feature, Fig. 1 left. In contrast, the eigenmodes of E_D^N and the vibration modes are sensitive to the feature, Fig. 1 middle and right. The eigenmodes of E_D^N corresponding to lower eigenvalues almost vanish at the feature and the vibration modes place additional extrema on the fold.

Investigating the differences between the eigenmodes of the Laplacian and E_D^N further, we compute them on the double torus with sharp features shown in Fig. 3. It can be seen that each of the shown Laplacian eigenmodes contains a more or less equally distributed set of extrema as well as a certain reflective symmetry, Fig. 3 left. The corresponding isolines suggest a low influence of the

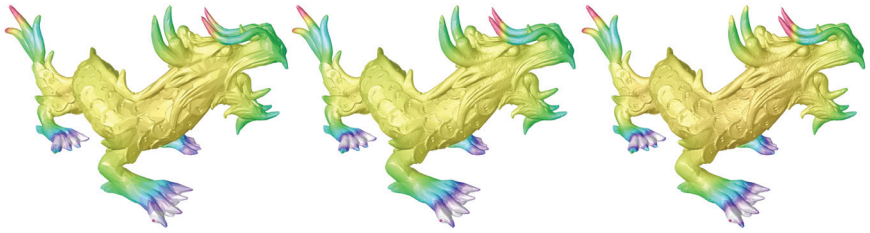

Figure 9: The thin-shell vibration distance computed on the dragon model in various resolutions: 10k, 50k, and 130k vertices. The results look similar which indicates that the distance can be well-approximated by computations on coarse meshes.

sharp features to the considered Laplacian eigenmodes. Similar to the Laplacian modes the two eigenmodes for E_D^N also posses a reflection symmetry, Fig. 3 right. But here we find that the eigenmodes of the lower part of the spectrum correspond to oscillations of flat areas surrounded by sharp edges, Fig. 3 right. This matches our considerations in Section 3.

Fig. 4 shows eigenvibrations with respect to the discrete thin shell energy. The images on the left (top and bottom row) show the reference mesh and each of the other images visualizes a vibration mode. The discrete thin shell energy is a weighted sum of a flexural and a membrane energy. If we decrease the weight of the membrane energy, the resulting vibration modes include stretching and squashing of the surface, Fig. 4 top row 2^{nd} and 3^{rd} image. In contrast, if we put a large weight on the membrane energy, the resulting eigenmodes try to preserve the metric. Examples of such modes are given in Fig. 4 top row 4^{th}, bottom row 2^{nd} and 3^{rd} image.

Vibration signature. In the following we examine the properties of the vibration signature S_t^{Vib} defined in eq. (27) and compare it to the heat kernel signature (HKS) introduced in Sun et al. (2009). As noted in Section 6, S_t^{Vib}(v) encodes the vibration behavior of a vertex v on multiple scales, *i.e.*, vertices that oscillate with similar intensity throughout the eigenmodes, will be close in terms of the vibration distance $\delta_{[t_1,t_2]}(\cdot,\cdot)$. We illustrate this property in Fig. 5 for the Armadillo model (16k vertices). On the left we color plot the vibration distance $\delta_{[t_1,t_2]}(v,\cdot)$ to the marked vertex v. Two further binary colorings are given, colorizing vertices that are closer to v than a threshold in blue and the other vertices in white. For a small threshold the vertices on both feet are close to v; increasing the threshold causes parts of the hands to be colored in blue as well.

Fig. 6 compares S_t^{Vib} to the HKS. Every image of the hand model (40k vertices) depicts the vertices that are closer to the marked vertex v. In the first column similar results are achieved for HKS and S_t^{Vib}. Since the HKS is constructed using the spectrum and eigenfunctions of the Laplacian, the signature depends only on intrinsic properties of the surface. Thus the signature is incapable of differentiating between isometrically deformed parts of a surface. The vibration signature however is sensitive to extrinsic information and hence

represents an alternative to the HKS. This characteristic of S_t^{Vib} becomes especially apparent in the second column of Fig. 6. Here the middle finger of the hand is almost isometrically deformed. The HKS cannot distinguish this situation from the undeformed one; hence it recognizes the tips of the three longest fingers of the hand as similar to vertex v. As the deformation alters the vibration behavior of the bent finger, S_t^{Vib} detects only the tips of the unbent ones. Like the HKS, the vibration distance can be evaluated at different scales (different choices of $[t_1, t_2]$). Choosing smaller values of t increases the weights (*cf.* eq. 27) for eigenmodes with higher frequency. Therefore, more local vibrations described by these eigenmodes contribute more to the vibration distance. An example is shown on the right side of the lower row of Fig. 6. For smaller t, $\delta_{[t_1,t_2]}(v, \cdot)$ captures vibrations of the fingertips as well and thus classifies the vertices on all tips as similar to v.

In Fig. 7 we provide a last comparison of the vibration signature and the HKS for the camel model (10k vertices). The vibration distance shown on the left, finds both pairs of knees (at the forelegs and at the hind legs) to be the closest to vertex v. For the HKS, shown on the right, the results are not as intuitive: the vertices at the mouth and ears of the camel are closer to the vertex v than the vertices at the hind legs, even closer than the vertices at the knees of the hind legs. This behavior of the HKS was the same at different scales and it is difficult to interpret the results. An indication for this behavior can be found by inspecting the Fiedler vector, which is the eigenfunction of the discrete Laplacian associated to the lowest (non-zero) eigenvalue. Of all eigenfunctions, this one gets the highest weight in the heat kernel distance. On the camel model, the Fiedler vector has one type of extrema (*e.g.* its minima) at tips of the toes of the hind legs at the tip of the tail and the other type of extrema (*e.g.* its maxima) at the tips of the toes of the forelegs, at the tips of the ears, and the tip of the snout. The function values at the tips of the ears and the tip of the snout are about the same as the function values at the knees of the forelegs. Hence, the contribution of this eigenfunction to the heat kernel distance is almost zero. This behavior repeats at some of the higher modes.

Feature signature. The feature signature and the feature distance can be used to identify features of the surface like sharp bends or sharp corners. It is our impression that the signature could serve as an indicator function to surface segmentation algorithms. Fig. 8 shows the feature signature on the rockerarm model for different scale values. Vertices of the mesh that have a signature value close to zero are colored white in these images. The white areas seem to include the important features of the rocker-arm model. The lower left image shows in blue all the vertices that are close (with respect to the feature distance) to a vertex on a sharp bend. For comparison we show a curvature plot ($\sqrt{\kappa_1^2 + \kappa_2^2}$) on the rocker-arm.

Concerning the applicability as a feature indicator, a nice aspect of the feature signature compared to curvature is that the feature signature *naturally* comes with a scale parameter, whereas for curvature a scale space needs to be constructed. Another interesting difference is the following. Some areas of the

rockerarm model have high curvature but do not indicate features, *e.g.*, the curved area inside the hole has a much higher curvature than for example the flat parts on the sides of the model. Still, the feature distance associates similar function values to both of these parts.

Figure 10: Features detected with our feature signature (blue) and the heat kernel signature (green) on a collection of models are shown.

Comparison of feature signature and heat kernel signature. Feature detection is an application that highlights differences between our feature signature and the heat kernel signature. This is due to the isometry invariance of the HKS, which implies that the HKS marks only features that remain features under arbitrary isometric deformations. For example, sharp bends (like the one

in Fig. 1) are not regarded as features by the HKS. Similar to the example shown in Fig. 8, we select an initial point and mark all points that are close to the initial point with respect to a modal distance. For comparison, Fig. 10 shows results obtained with our feature distance (colored in blue) and with the heat kernel distance (colored in green) on a collection of models. The first example, the blade model (top left) shows the features detected for three different initial points located on corners and sharp bends of the surface. Whereas the feature signature finds almost identical sets of feature for all three initial points, the results the HKS produces vary strongly. On the turbocharger model (top right) we select two different initial points, one located on a sharp bend and one point close to a bend. The images show that in the second case the feature signature marks points that have similar distance to a feature as the initial point. Since the sharp bends on this surface are curved (in the tangential direction orthogonal to the bend), the HKS detects these features as well and produces comparable results to the feature signature. A second example where the feature signature and the HKS produce similar results is the bumpy plate (bottom right).

Implementation details and timings. The computation of the eigenmodes and eigenvalues of an energy splits in two steps: setting up the Hessian matrix and solving the eigenproblem. To compute the signatures and distances, we additionally need to evaluate formulae (27) (resp. (30)) and (31). Lemma 1 simplifies and accelerates the construction of the Hessians such that the time required for this step is negligible compared to the computation of the eigenmodes. Based on the lemma, we implemented an explicit formula for the Hessian of the energies at the rest state, alternatively automatic differentiation can be used. In the second step, we need to solve a sparse generalized eigenproblem. One way to solve such a generalized eigenvalue problem is to transform it to a standard eigenvalue problem. In our case the mass matrix is a positive definite diagonal matrix, therefore such a basis transformation requires only rescaling of the Lagrange basis vectors. Details for this procedure can be found in Vallet and Lévy (2008). To compute the signatures and distance, only a fraction of the lower part is required, because the weights $e^{-\lambda_j t}$ rapidly decrease with increasing eigenvalue. Typically the first 300 eigenvalues and modes yield a faithful approximation of the signatures and distances. To efficiently compute a lower portion of the spectrum and its corresponding eigenvectors we employ the shift-and-invert Lanczos method which does not need the inverse matrix explicitly. Instead only a matrix vector product has to be provided which can be evaluated by solving a linear system of equations. We solve these systems using the sparse direct solver implemented in *MUMPS*, see Amestoy et al. (2001). Once the eigenvalues are computed, the evaluation of the signatures and distances is relatively fast. To discretize the integral in (31), we use a numeric quadrature. We place the samples of the interval $[t_1, t_2]$ such that they are equidistant on the logarithmic scale, which yields equal weights for all points in the quadrature.

In our experiments, we found that coarse meshes already provide a good approximation of the eigenmodes of the energy. Hence, for applications where

computation time is crucial, it seems reasonable to first sub-sample the mesh and to compute the spectrum and eigenvectors of the simplified model. Fig. 9 shows similarity results of the vibration distance for the Chinese dragon model at different mesh-resolutions. Although the model is simplified significantly, the similarity results still resemble the results of the fine mesh, indicating that the signature and the distance can be well-approximation on coarse meshes. Table 1 provides timings for computing the vibration signature of different versions of the Chinese dragon model.

Model	#Vertices	Hessian	Eigenproblem	S_t^{Vib}
Dragon (Fig. 9, left)	10k	1 s	58 s	4 s
Dragon (Fig. 9, middle)	50k	4 s	326 s	30 s
Dragon (Fig. 9, right)	130k	11 s	1122 s	100 s

Table 1: Timings for the chinese dragon model measured on a custom Macbook Pro with a 2.66GHz CPU. From left to right: model, number of vertices, timings in seconds for constructing the Hessian, solving the eigenproblem, and computing the vibration signature at all points.

8. Future Work

Our future work relates to the problem of spectral quadrangulations. In contrast to the modes of the Laplacian, the modes of the energies considered in this work are sensitive to the extrinsic curvature of the surface. Our goal is to produce quadrangualtions that align with salient surface features. Furthermore, after submission of this paper we have developed a method that uses the vibration modes and their modal derivatives to create a subspace of the shape space of a mesh. Then, this subspace is used to speed up deformation-based modeling of surfaces. Our results can be found in Hildebrandt et al. (2011).

Acknowledgements. We would like to the anonymous reviewers for their helpful comments and suggestions. This work was supported by the DFG Research Center Matheon "Mathematics for Key Technologies" in Berlin.

References

Amestoy, P.R., Duff, I.S., Koster, J., L'Excellent, J.Y., 2001. A fully asynchronous multifrontal solver using distributed dynamic scheduling. SIAM Journal on Matrix Analysis and Applications 23, 15–41.

Baraff, D., Witkin, A., 1998. Large steps in cloth simulation, in: Proceedings of ACM SIGGRAPH, pp. 43–54.

Barbič, J., James, D.L., 2005. Real-time subspace integration for St. Venant-Kirchhoff deformable models. ACM Transactions on Graphics 24, 982–990.

Bridson, R., Marino, S., Fedkiw, R., 2003. Simulation of clothing with folds and wrinkles, in: Proceedings of ACM SIGGRAPH/Eurographics Symposium on Computer Animation, pp. 28–36.

Choi, M.G., Ko, H.S., 2005. Modal warping: Real-time simulation of large rotational deformation and manipulation. IEEE Transactions on Visualization and Computer Graphics 11, 91–101.

Clarenz, U., Diewald, U., Dziuk, G., Rumpf, M., Rusu, R., 2004. A finite element method for surface restoration with smooth boundary conditions. Comput. Aided Geom. Des. 21, 427–445.

Dey, T.K., Li, K., Luo, C., Ranjan, P., Safa, I., Wang, Y., 2010. Persistent heat signature for pose-oblivious matching of incomplete models. Computer Graphics Forum 29, 1545–1554.

Dong, S., Bremer, P.T., Garland, M., Pascucci, V., Hart, J.C., 2006. Spectral surface quadrangulation. ACM Transactions on Graphics 25, 1057–1066.

Dziuk, G., 1988. Finite elements for the Beltrami operator on arbitrary surfaces, in: Partial Differential Equations and Calculus of Variations. Springer. volume 1357 of *Lecture Notes in Mathematics*, pp. 142–155.

Dziuk, G., 1991. An algorithm for evolutionary surfaces. Numer. Math. 58 , 603–611.

Eckstein, I., Pons, J.P., Tong, Y., Kuo, C.C.J., Desbrun, M., 2007. Generalized surface flows for mesh processing, in: Symposium on Geometry Processing, Eurographics Association. pp. 183–192.

Garg, A., Grinspun, E., Wardetzky, M., Zorin, D., 2007. Cubic Shells, in: Proceedings of ACM SIGGRAPH/Eurographics Symposium on Computer Animation, pp. 91–98.

Gebal, K., Bærentzen, J.A., Aanæs, H., Larsen, R., 2009. Shape analysis using the auto diffusion function. Computer Graphics Forum 28, 1405–1413.

Grinspun, E., Hirani, A.N., Desbrun, M., Schröder, P., 2003. Discrete shells, in: Proceedings of ACM SIGGRAPH/Eurographics Symposium on Computer Animation, pp. 62–67.

Hauser, K.K., Shen, C., O'Brien, J.F., 2003. Interactive deformation using modal analysis with constraints, in: Graphics Interface, pp. 247–256.

Hildebrandt, K., Polthier, K., Wardetzky, M., 2006. On the convergence of metric and geometric properties of polyhedral surfaces. Geometricae Dedicata 123, 89–112.

Hildebrandt, K., Schulz, C., von Tycowicz, C., Polthier, K., 2011. Interactive surface modeling using modal analysis. ACM Trans. Graph. 30, 119:1–119:11.

Huang, J., Zhang, M., Ma, J., Liu, X., Kobbelt, L., Bao, H., 2008. Spectral quadrangulation with orientation and alignment control. ACM Transactions on Graphics 27, 1–9.

Huang, Q., Wicke, M., Adams, B., Guibas, L., 2009. Shape decomposition using modal analysis. Computer Graphics Forum 28, 407–416.

Jost, J., 2008. Riemannian geometry and geometric analysis. Springer Verlag.

Lehoucq, R.B., Sorensen, D.C., Yang, C., 1998. ARPACK users' guide - solution of large-scale eigenvalue problems with implicitly restarted Arnoldi methods. Software, environments, tools, SIAM.

Lévy, B., Zhang, H., 2009. Spectral mesh processing, in: ACM SIGGRAPH ASIA Courses, pp. 1–47.

Ovsjanikov, M., Mérigot, Q., Mémoli, F., Guibas, L., 2010. One point isometric matching with the heat kernel. Computer Graphics Forum 29, 1555–1564.

Ovsjanikov, M., Sun, J., Guibas, L., 2008. Global intrinsic symmetries of shapes. Computer Graphics Forum 27, 1341–1348.

Pentland, A., Williams, J., 1989. Good vibrations: modal dynamics for graphics and animation, in: Proceedings of ACM SIGGRAPH, pp. 215–222.

Pinkall, U., Polthier, K., 1993. Computing discrete minimal surfaces and their conjugates. Experimental Mathematics 2, 15–36.

Polthier, K., 2005. Computational aspects of discrete minimal surfaces, in: Hass, J., Hoffman, D., Jaffe, A., Rosenberg, H., Schoen, R., Wolf, M. (Eds.), Global Theory of Minimal Surfaces, Clay Foundation.

Reuter, M., Wolter, F.E., Peinecke, N., 2005. Laplace-spectra as fingerprints for shape matching, in: Proceedings of the ACM Symposium on Solid and Physical Modeling, pp. 101–106.

Reuter, M., Wolter, F.E., Peinecke, N., 2006. Laplace-Beltrami spectra as "Shape-DNA" of surfaces and solids. Computer-Aided Design 38, 342–366.

Rustamov, R.M., 2007. Laplace-Beltrami eigenfunctions for deformation invariant shape representation, in: Proceedings of Eurographics/ACM SIGGRAPH Symposium on Geometry Processing, pp. 225–233.

Saad, Y., 1992. Numerical Methods for Large Eigenvalue Problems. Manchester University Press.

Sorkine, O., Alexa, M., 2007. As-rigid-as-possible surface modeling, in: Proceedings of Eurographics/ACM SIGGRAPH Symposium on Geometry Processing, pp. 109–116.

Sun, J., Ovsjanikov, M., Guibas, L.J., 2009. A concise and provably informative multi-scale signature based on heat diffusion. Computer Graphics Forum 28, 1383–1392.

Vallet, B., Lévy, B., 2008. Spectral geometry processing with manifold harmonics. Computer Graphics Forum .

Wardetzky, M., Bergou, M., Harmon, D., Zorin, D., Grinspun, E., 2007. Discrete quadratic curvature energies. Computer Aided Geometric Design 24, 499–518.

Zhang, H., van Kaick, O., Dyer, R., 2010. Spectral mesh processing. Computer Graphics Forum To appear.